Journal of Materials Chemistry A

ROYAL SOCIETY OF CHEMISTRY

PAPER

View Article Online
View Journal | View Issue

Check for updates

Cite this: J. Mater. Chem. A, 2024, 12, 23810

High lithiophilicity and Li diffusion rate on 1T phase transition metal dichalcogenides as effective Li regulating materials for dendrite-free metal anodes†

Hoilun Wong, Md Delowar Hossain, Mengyang Xu, Yuting Cai, Mohsen Tamtaji, Kenan Zhang and Zhengtang Luo *

Received 28th May 2024
Accepted 22nd July 2024

DOI: 10.1039/d4ta03686g

rsc.li/materials-a

Effective lithium regulating materials (LRMs) that enable fast Li diffusion, as well as regulate Li nucleation to avoid its aggregation, are promising to eliminate the uncontrolled dendrite formation at the metal anode. Herein, we find that the 1T phase transition metal sulfides and selenides are a good LRM for Li metal anode *via* systematic investigation on Li binding strength and diffusion barrier, experimentally and computationally, among a series of 2D materials, including graphene, h-BN and 20 transition metal sulfides/selenides. The high Li binding strength arises from the high and concentrated charge transfer to Li due to the high electronegativity and local dipole of metal sulfides and selenides. To validate the result, 2D VS_2 flakes were synthesized on nitrogen-doped CNT (NCNT) using the chemical vapor deposition (CVD) method. The symmetric Li/Li cells using VS_2-LRM exhibited excellent cyclic stability over 1000 cycles with low overpotentials of 75 and 12 mV at 0.5 and 2 mA cm^{-2}, respectively, with uniform and compact Li deposition. This work provides a fundamental understanding of designing efficient LRMs for a dendrite-free metal anode and uncovers the lithiophilicity chemistry of 2D metal sulfides/selenides for safe rechargeable metal batteries.

1. Introduction

Compared to the conventional graphite-intercalated materials in lithium-ion batteries (LIBs), lithium metal has been considered an ideal anode material for rechargeable batteries owing to its ultrahigh theoretical specific capacity of 3860 mA h g^{-1} and the lowest redox potential (−3.04 V *vs.* standard hydrogen electrode).[1–3] However, the Li dendrite formation amid the Li plating/stripping process causes unfavorable electrolyte drying, loss of "dead Li" and dendrite penetration through a separator to the cathode, resulting in poor cell cyclability, low coulombic efficiency, internal short circuit and safety issues, hurdling the practical applications of LMBs.[4] Replacing the liquid electrolytes with solid-state electrolytes is a successful way to reduce the safety hazards, avoid forming complicated solid electrolyte interfaces (SEIs) and inhibit dendrite propagation.[5–7] However, it is challenging to significantly improve the poor ionic conductivity of the solid electrolyte ($\sim 10^{-8}$ to 10^{-4} S cm^{-1}), compared to the liquid electrolyte ($\sim 10^{-3}$ S cm^{-1}).[8] In addition, Li–X (X = Al, B, Si, Mg)[9–12] alloy approaches alter the Li deposition behaviors by replacing Li from a metallic state to an ionic state, obtaining a smoother metal deposition. Unfortunately, large volume change during cycling pulverizes the electrode structure and thus deteriorates the cyclability. Various electrolyte additives such as fluoroethylene carbonate,[13] $LiNO_3$,[14] and $LiPF_6$ (ref. 15) have been used to form an artificial SEI layer on the electrode surface to prevent irregular dendrite deposition. Nevertheless, the stability of these thin protective layers is poor along the cycling.

Previous fundamental studies, including modelling and experimental works, showed three vital dendrite plating phenomena: (1) Li dendrite preferentially germinates from cracks, metal grains and defects, unavoidably induced by dislocation displacement along crystallographic planes, as the result of mechanical stress.[16] (2) Inhomogeneity and brittleness of the SEI layer intrinsically triggers the dendrite growth and (3) dendrite growth is always facilitated on the protrusions.[17–19] In principle, Li dendrite formation is natural and difficult to prevent. Instead, by introducing effective Li regulating materials (LRMs), such as metals (Ag, Au and Mg),[20–22] functionalized carbon materials (heteroatom and single-atom-doped graphene)[17,23,24] and MoS_2,[25] researchers were able to control the Li nucleation sites and regulate the dendrite growth direction, a preferable strategy to address the dendrite issues[26–28] (Fig. 1).

Department of Chemical and Biological Engineering, William Mong Institute of Nano Science and Technology, Hong Kong University of Science and Technology, Clear Water Bay, Kowloon, Hong Kong. E-mail: keztluo@ust.hk

† Electronic supplementary information (ESI) available. See DOI: https://doi.org/10.1039/d4ta03686g

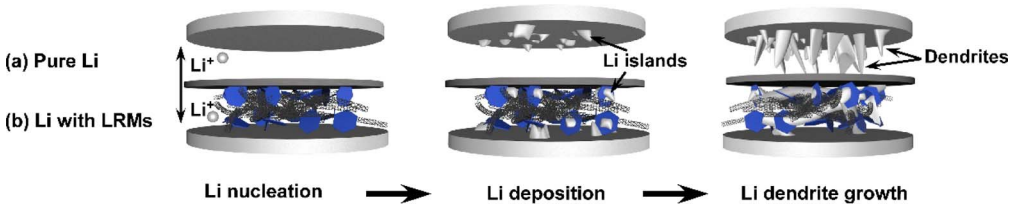

Fig. 1 Schematic of Li nucleation, deposition and dendrite growth in cells with and without LRMs. The cell with (a) pure Li and (b) Li with LRMs. The illustration explains the achievement of dendrite-free Li deposition with our LRMs coating on a separator.

Inspired by the above strategies, the polar materials 2D transition metal dichalcogenides (TMDs) on graphene framework not only provide excellent lithiophilicity at the sulfide/selenide sites, but also enable low Li diffusion barrier, considered as perfect LRMs to regulate Li nucleation, and thus effectively suppress the dendrite growth. In this work, we studied a broad range of TMDs (TiS_2, $TiSe_2$, VS_2, VSe_2, CrS_2, $CrSe_2$, CoS_2, NiS_2, NbS_2, $NbSe_2$, MoS_2, $MoSe_2$, TaS_2, $TaSe_2$, WS_2, WSe_2, ReS_2, $ReSe_2$, PtS_2, and $PtSe_2$), utilizing theoretical calculations of density functional theory (DFT) to calculate their (i) Li binding strengths and (ii) lithium diffusivities. We found that all TMDs except WSe_2 are able to regulate the Li nucleation, while 1T phase metal sulfides/selenides exhibited significantly higher Li binding strength and lower Li diffusion barrier than the 2H phase, while both outperformed graphene and h-BN. Besides, we also found that transition metal sulfides would offer higher Li affinity than metal selenides and follow the Li affinity trend of TMDs with transition metals 3d > 4d > 5d. For the Li diffusivity, 1T phase metal sulfides/selenides generally enable faster Li diffusion than the 2H phase, and all phases perform better than the pure graphene. Furthermore, VS_2 was synthesized on nitrogen-doped carbon nanotubes (VS_2/NCNT) to represent the TMDs using the chemical vapor deposition (CVD) method. Carbon nanotubes are used as the high-surface conductive substrate for Li deposition, while VS_2 crystals in the composite offer strong Li binding energy to regulate the Li^+ ion nucleation. A uniform and compact Li deposition was obtained with the VS_2/NCNT composite and was tested in symmetric Li/Li cells. Our results demonstrated excellent cycling stability with <100 mV deposition overpotential of over 1000 h at current densities of 0.5 and 2.0 mA cm^{-2} and the deposition capacities of 1.0 and 2.0 mA h cm^{-2}, respectively, which was verified from our calculation results.

2. Results and discussion

Firstly, DFT calculations were performed to study two material properties of Li binding strength and diffusion barrier. Fig. 2a–f and S1† show the optimized configuration in that the Li atom is adsorbed at the most energy favourable site on LRM's surfaces and the two metal surfaces of Li (001) and Cu (111). For the graphene surface, the Li atom is preferably adsorbed at the hollow carbon site. For h-BN, the preferential Li binding site is on top of the nitrogen within the B–N skeleton. For 2H and 1T TMDs, in most cases, the Li atom is energetically adsorbed on the metal sites. In Fig. 2g, the Li binding energy on Li (001) is −1.44 eV, used as the reference to indicate the Li dendrite formation. LRM with energy that is lower than −1.44 eV, is regarded as a good material for regulating the Li nucleation. The binding energies on h-BN (−0.28 eV), pristine graphene (−1.12 eV) and WSe_2 (−1.35 eV) are higher than those of the reference, indicating weak interaction, which promoted the Li atom aggregation to form dendrites. In comparison, the Li binding energy on Cu (111), TiS_2, VS_2, CrS_2, CoS_2, NiS_2, NbS_2, MoS_2, TaS_2, WS_2, ReS_2, PtS_2, $TiSe_2$, VSe_2, $CrSe_2$, $NbSe_2$, $MoSe_2$, $TaSe_2$, $ReSe_2$ and $PtSe_2$ are −2.54, −3.62, −3.41, −4.07, −4.26, −3.08, −3.94, −1.94, −3.75, −1.57, −2.02, −2.33, −3.21, −2.98, −3.50, −3.50, −1.66, −3.35, −2.64 and −2.20 eV, respectively, and higher binding strength than that of Li (001), are, therefore, considered as the better LRMs to guide the Li nucleation.

As shown in Fig. 3a, we found that the 1T phase metal sulfides and selenides offer a slightly stronger Li affinity than the 2H phase, able to navigate the Li nucleation direction, leading to a more regular Li deposition behaviour. In addition, transition metal sulfides (blue) generally provide stronger Li binding energy than the metal selenides (orange) (Fig. 3b), while the Li binding strength decreases with increasing number of d orbitals in Fig. 3c.

Bader charge analysis was performed to explain the Li binding study described in Fig. 4. The charge transfer between Li and the substrates is denoted as Li/h-BN, Li/graphene and Li/VS_2. The Bader charge profile shows that only 0.008 e per atom charge is transferred from Li to h-BN (Fig. 4a), indicating a very weak binding strength of 0.28 eV, while for Li/graphene and Li/VS_2 systems, 0.027 and 0.032 e per atom of charges are shared by an Li atom, respectively and lead to a stronger Li affinity. Furthermore, it is noteworthy that the charge accumulation is more concentrated in Li/VS_2, but dispersed in Li/graphene from Fig. 4b and c, implying that the interaction between Li and VS_2 is much stronger. Compared to graphene, ion-dipole force is formed between the transition metal and sulfur and selenium atoms in TMDs, delivering an induced dipole towards the adsorbed Li^+ ions (Tables S1 and S2†). The less electronegative the metal ion, the stronger the local dipole is created at S/Se atoms to adsorb Li. Therefore, electronegativity is one of the good indicators of Li affinity. For example, compared to Mo (2.16), W (2.36) and V (1.63) are less electronegative that a stronger ion-dipole force is generated at S (2.58) than at Se (2.55) atoms to attract Li, thereby VS_2 provides the stronger navigating power than MoS_2 and WS_2 to guide Li nucleation. An implicit correlation between Li binding energy and a descriptor

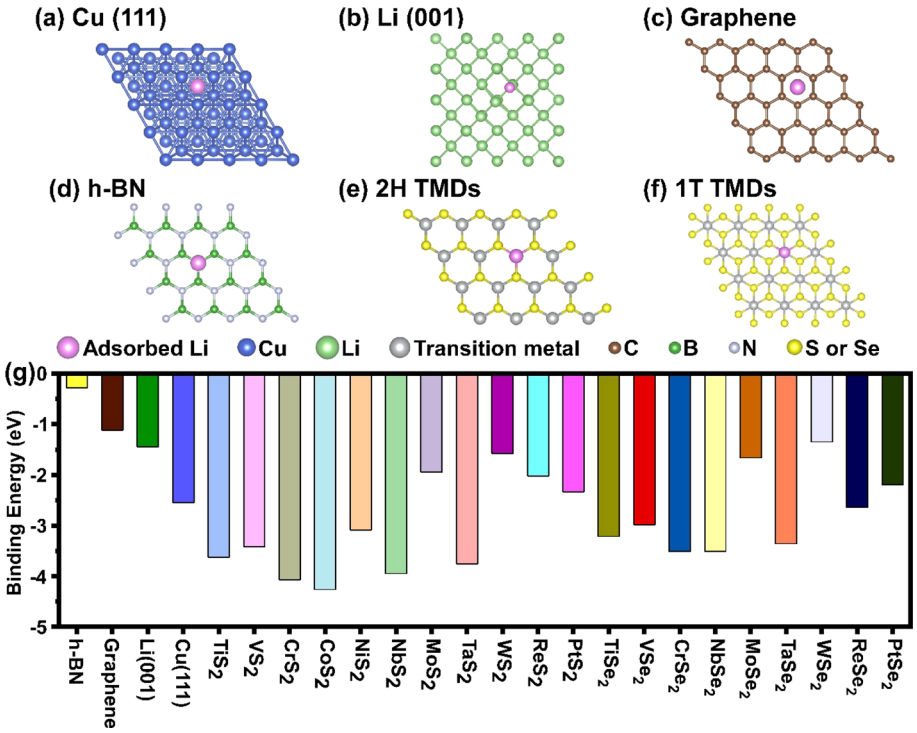

Fig. 2 Li binding Study. (a–f) Optimized structures of Li atom adsorbed on the LRM's surfaces. (g) Comparison of the Li binding energy of studied TMDs to that of h-BN, graphene, Li (001) and Cu (111).

of $\Phi = EN \times \dfrac{\text{period number of transition metal}}{\dfrac{\text{atomic radius of S or Se}}{10}}$, is proposed in Fig. 4d. The metal sulfides/selenides with higher charge density and smaller metal electronegativity deliver higher Li binding strength.

Li diffusivity is an important characteristic of dendrite formation, as a lower diffusion barrier would enable a faster Li transport, leading to a uniform Li deposition. A climbing image nudged elastic band (CI-NEB) was performed to calculate the Li diffusion barrier. Fig. 5a–d illustrates the diffusion pathways of Li on the surfaces of graphene, h-BN, MoS_2 and VS_2. For graphene and h-BN, the diffusion paths start and end at the most stable positions of the center of the hexagonal carbon ring and nitrogen atom, respectively, along a straight path. In contrast, the diffusion paths of 2H MoS_2 and 1T VS_2 start and end at the metal positions, along the "V-shaped" path. As shown in Fig. 5e, one peak was observed in the diffusion path of graphene and h-BN and in contrast two peak points are observed for MoS_2 and VS_2, forming an "M-shaped" curve. The diffusion barriers of Li on graphene and h-BN are 0.291 and 0.007 eV, respectively, and the result indicates that the diffusion barriers of all metal sulfides and selenides are smaller than that of 0.29 eV on graphene, evidencing a faster diffusion rate on 2D metal sulfides and selenides than on graphene. Among the 20 transition metal sulfides and selenides, the Li diffusion barriers on the 2H phase NbS_2, MoS_2, TaS_2, WS_2, ReS_2, $NbSe_2$, $MoSe_2$, $TaSe_2$ and WSe_2 are

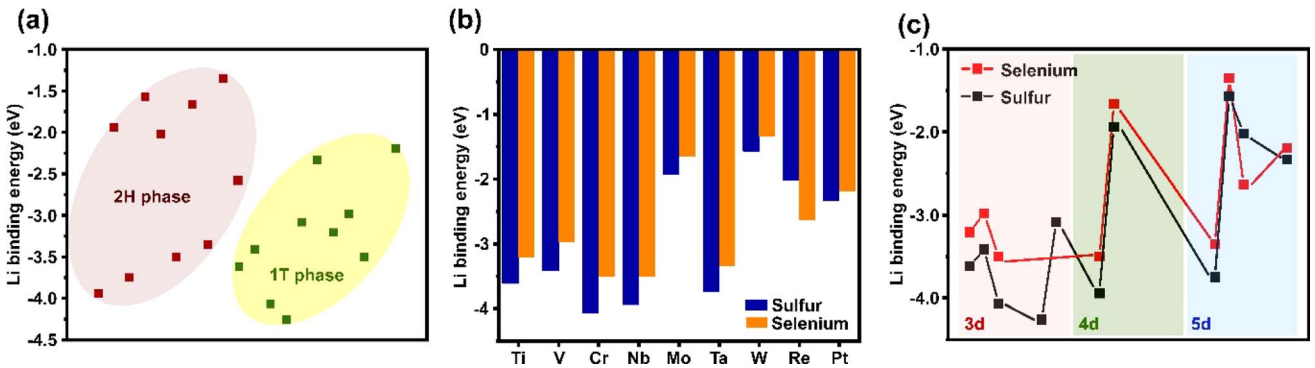

Fig. 3 Analysis of Li binding results. Comparison of Li binding energy between (a) 2H and 1T phases of TMDs, (b) transition metal sulfides and selenides, and (c) over number of d orbitals of transition metal in TMDs.

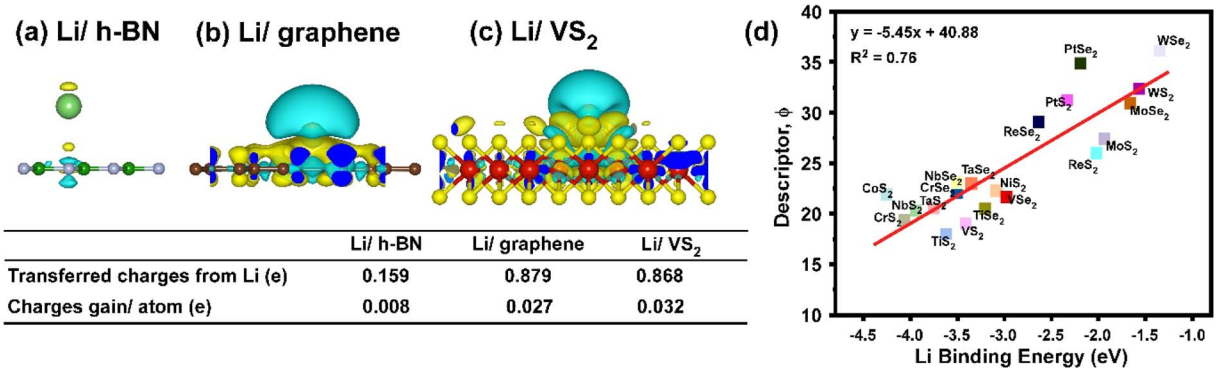

	Li/ h-BN	Li/ graphene	Li/ VS_2
Transferred charges from Li (e)	0.159	0.879	0.868
Charges gain/ atom (e)	0.008	0.027	0.032

Fig. 4 Bader charge analysis and the principle of designing lithiophilic LRMs. Side view of charge transfer within the system of (a) Li/h-BN, (b) Li/graphene and (c) Li/VS_2 (isosurface value = 0.0006 e Å^{-3}) yellow and cyan colors represent the charge availability and deficiency, respectively. A higher and more concentrated charge is transferred in Li/VS_2, indicating a stronger interaction between Li and VS_2. (d) The correlation between *f* and Li binding energy.

0.181, 0.253, 0.188, 0.247, 0.122, 0.196, 0.260, 0.206 and 0.244 eV, respectively. Fig. 5f shows that the Li diffusion barrier of 2H phase transition metal sulfides and selenides is slightly higher than that of 1T phase TiS_2 (0.199 eV), VS_2 (0.195 eV), CrS_2 (0.150 eV), CoS_2 (0.180 eV), NiS_2 (0.219 eV), PtS_2 (0.166 eV), $TiSe_2$ (0.206 eV), VSe_2 (0.165 eV), $CrSe_2$ (0.090 eV) and $PtSe_2$ (0.217 eV). Notably, the Li diffusion barrier is determined by measuring the largest binding energy difference of selected diffusion points along the whole pathway. For example, for VS_2, 10 diffusion points were calculated along the path and among these, the largest energy difference was between the initial and third points, *i.e.* 0.195 eV.

Based on the above computational studies, we find that the 1T phase metal sulfides and selenides are the preferable LRMs for the lithium metal anode. Following the previously reported methods from our group,[29] hexagonal VS_2 crystals are synthesized to represent the 1T TMDs for the experimental part. As illustrated in Fig. 6a, VS_2 is fabricated on polydopamine-coated CNT (shown in Fig. S2†) using the CVD method, denoted as VS_2/NCNT and further coated on a separator for battery testing. The morphology and structure of VS_2/NCNT are characterized by

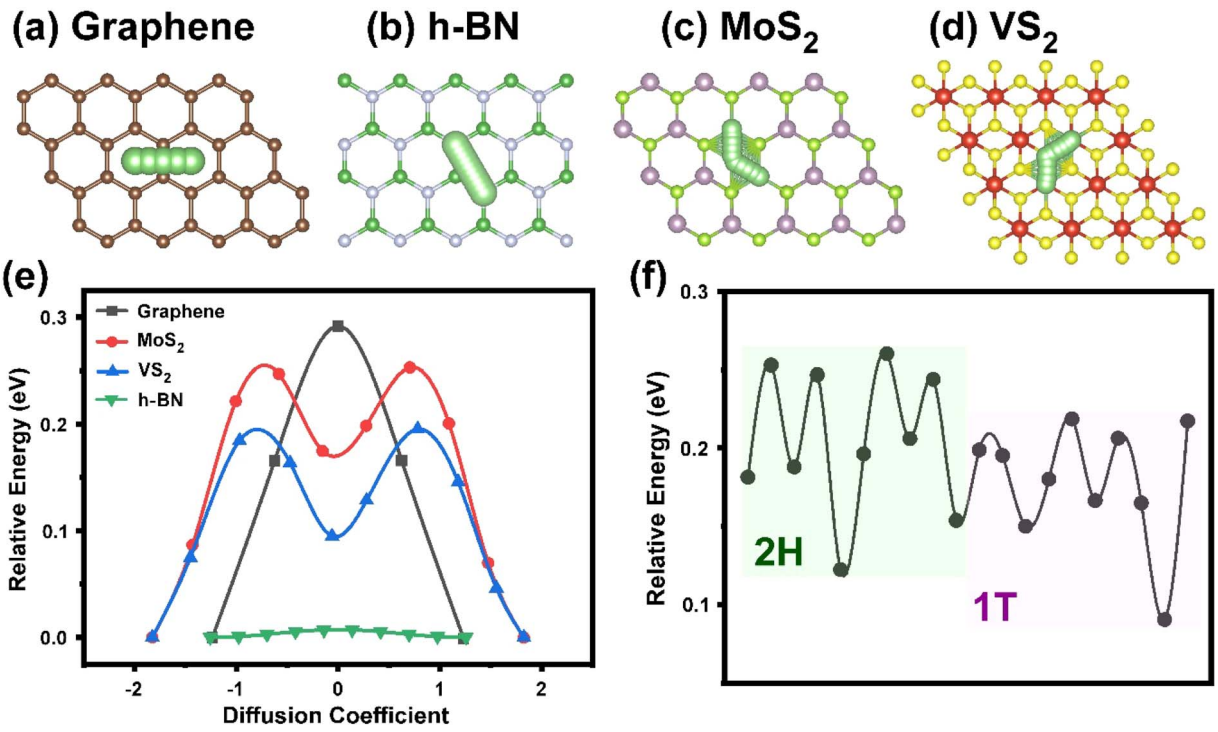

Fig. 5 Potential energy profile of Li atom diffusion on the surfaces. Top views of the optimized Li atom diffusion pathways on (a) graphene, (b) h-BN, (c) MoS_2 and (d) VS_2. (e) Comparison of Li diffusion barrier of graphene, MoS_2, VS_2 and h-BN and (f) between 2H and 1T transition metal sulfides and selenides.

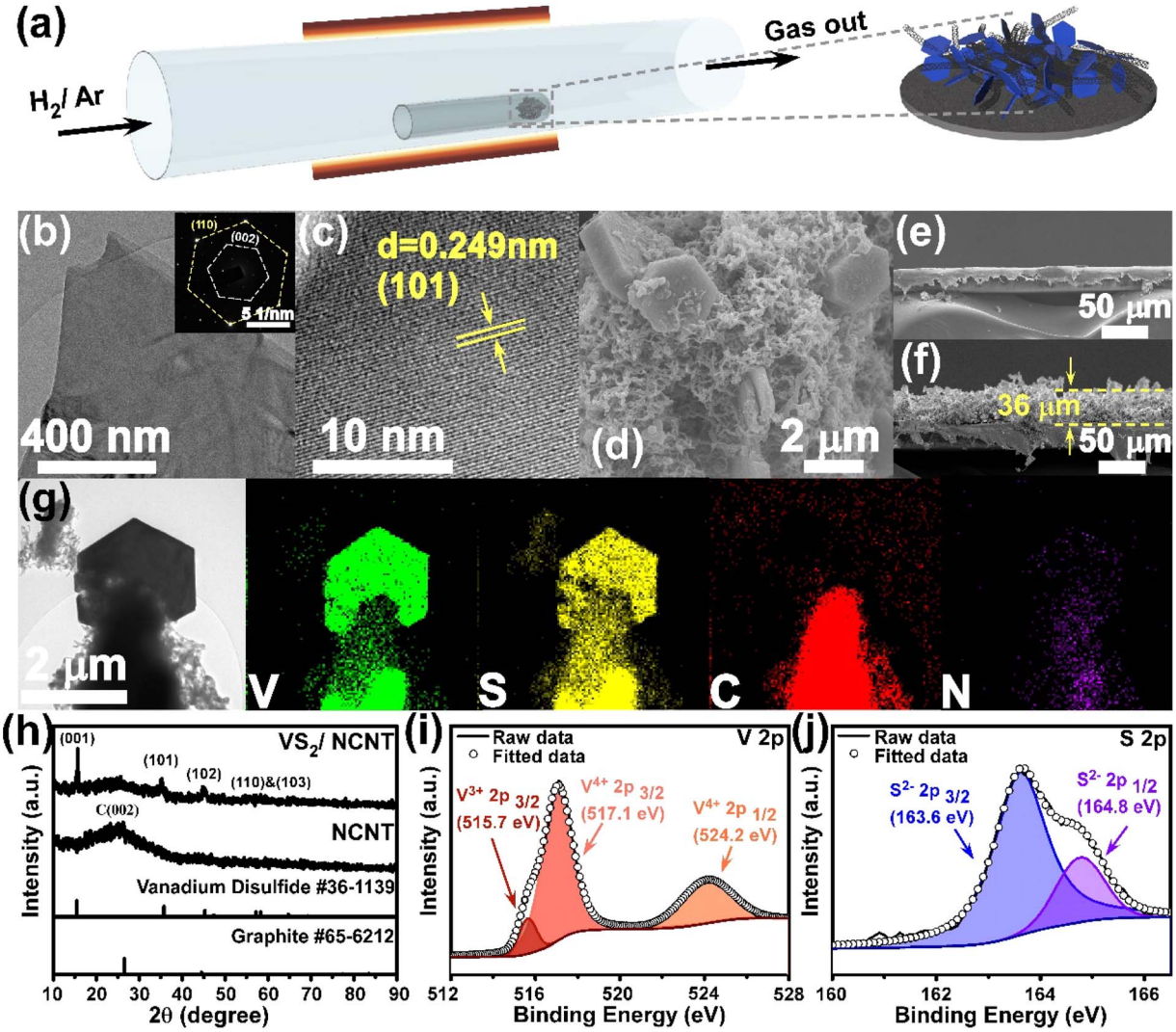

Fig. 6 VS_2 fabrication process, structure and elemental characterizations. (a) Schematics of the growth of VS_2 on NCNT, coated on a separator. (b) TEM image of the VS_2 flake. The inset is the SAED pattern of VS_2. (c) HRTEM image of VS_2 indicating the (101) crystal plane. (d) SEM image of VS_2/NCNT composite. Cross-section SEM images of (e) blank separator and (f) VS_2/NCNT modified separator. (g) Low-magnification TEM image of VS_2/NCNT with elemental mapping of V, S, C and N. (h) XRD patterns of VS_2/NCNT and CNT compared with the standard data of VS_2 and graphite. High-resolution XPS spectra of (i) V 2p and (j) S 2p. Single crystal of hexagonal VS_2 fakes synthesized on nitrogen-doped CNT.

transmission electron microscopy (TEM) and SEM. Fig. 6b shows the top view of a few-layered thick VS_2 sheet with the inset of a selected area diffraction (SAED) pattern, that presents the high quality and crystallinity of VS_2. The *d*-spacings measured from the diffraction points are 0.28 and 0.16 nm, representing (002) and (110) VS_2 crystal planes, respectively.[30] The high-resolution TEM image in Fig. 6c shows a lattice fringe with an interlayer distance of 0.249 nm, corresponding to the (101) plane of VS_2.[31] The composite of VS_2/NCNT (Fig. 6d) is coated on the PP separator by simple vacuum filtration. The side view of the SEM images (Fig. 6e and f) shows that VS_2/NCNT are uniformly coated on the separator with a thickness of ~36 mm. As shown in Fig. 6g, the energy-dispersive spectroscopy (EDS) mapping based on the TEM image was performed, indicating the elemental composition of V, S, C and N in the composite. The highly overlapped V and S signals at the hexagonal area identify the VS_2. Besides, the uniform N signals illustrate a uniform dispersion of nitrogen doping over the CNT substrate. Moreover, the VS_2 loading in the composite is 3.1% from the thermogravimetric analysis (TGA) result (Fig. S3†).

The crystal structure of VS_2/NCNT was further examined by X-ray diffraction (XRD). In Fig. 6h, a broad peak at around 26° was found in both the XRD patterns of VS_2/NCNT and NCNT, corresponding to the (002) lattice plane of CNT.[32] The distinct peaks at 15.6°, 35.2° and 45.1° are attributed to the (001), (101) and (102) crystal planes, respectively, of VS_2 (JCPDS card number: 36-1139). In addition, X-ray photoelectron spectroscopy (XPS) was carried out to study the elemental composition and the valence state of VS_2/NCNT. The full XPS spectrum (Fig. S4a†) displays six main peaks at 162, 282, 398, 516, 530 and 630 eV, representing the signal for S 2p, C 1s, N 1s, V 2p, O 1s and V 2s, respectively.[33] High resolution 2p spectra of V, S and 1s

spectrum N are shown in Fig. 6i, j and S4b,† respectively. In Fig. 6i, the peaks at 517.1 and 524.2 eV suggest the +4 oxidation state of V in the sample. A weak peak at 515.7 eV is observed and associated with V^{3+} $2p_{3/2}$. For the S 2p XPS spectrum in Fig. 6j, two strong peaks with the energy of 163.6 and 164.8 eV are ascribed S $2p_{3/2}$ and S $2p_{1/2}$, respectively, confirming the −2 oxidation state of S.[34,35] In addition, the N XPS spectrum in Fig. S4b† identifies three types of nitrogen doping with the peak at 398.4, 400.2 and 401.8 eV, describing pyridinic N, pyrrolic N and graphitic N, respectively. The composite material was coated on the separator and assembled into the Li/Li cell to check the Li deposition morphology and cycling performance.

To observe the Li deposition behaviors and morphologies, Li was electrically plated on both blank Cu and VS_2/NCNT/Cu at a high current density of 10 mA cm^{-2}. For VS_2/NCNT/Cu, the composite material of VS_2/NCNT was firstly blade cast on the Cu foil, followed by Li electrodeposition. Interestingly, nearly zero nucleation potential was found on VS_2/NCNT/Cu (Fig. S5a†), suggesting a low nucleation barrier. Rather, a large voltage dip (circled in red) was observed on Cu (Fig. S5b†), which indicated a high Li nucleation overpotential (54 mV), ascribed to large thermodynamics mismatch between Li and Cu.[22] Fig. 7a and b illustrate the SEM images of the samples of blank Cu and VS_2/NCNT/Cu after the Li electrodeposition at 0.5, 1.5 and 3.0 mA h cm^{-2}, respectively. At such a high current rate, uneven and finger-like dendrites are remarkably grown on blank Cu and become thick when the Li capacity is increased from 0.5 to 1.5 and 3.0 mA h cm^{-2}. It is noted that although the 1% $LiNO_3$ electrolyte additive was added to the electrolyte to strengthen the SEI surface and therefore improve the stability of the electrode, Li dendrites were still formed everywhere on the blank Cu, due to uneven current distribution. In comparison, with the composite of VS_2/NCNT, a smoother and more compact Li deposition surface was found. More specifically, when we applied the areal capacity of 0.5 mA h cm^{-2}, darker regions were identified and indicated the Li deposition within the composite layers. When we increased the areal capacity to 1.5 mA h cm^{-2}, more Li was deposited on VS_2/NCNT/Cu and some Li started growing outside of the coating layers onto the surface. Note that at 3.0 mA h cm^{-2}, Li deposition was still compact and dendrite-free, attributed to the benefits of VS_2/NCNT. The roughness of the surface was due to the coating of VS_2/NCNT.

To demonstrate the role of VS_2/NCNT in cycling performance, long-term electrochemical tests of Li plating/stripping in Li/Li symmetric cells with a blank separator and a VS_2/NCNT/separator were studied. When the cells were charged/discharged at 0.5 mA cm^{-2} areal current (Fig. 8a), the VS_2/NCNT/separator presented a flat voltage plateau with a low overpotential of 142 mV, indicating excellent stability. In comparison, significant overpotential variations were observed on a blank separator during cycling with a 7 times higher overpotential of 775 mV. Similarly, as shown in Fig. 8b and c, when the cells were charged faster at 2 mA cm^{-2}, a VS_2/NCNT/separator exhibited better stability with overpotentials of 265 and 380 mV for 1 and 2 mA h cm^{-2} Li deposition, respectively. However, a blank separator suffers from larger polarizations of 591 mV and 2.73 V for 1 and 2 mA h cm^{-2} Li deposition, respectively. This verifies our calculation results that the VS_2/NCNT/separator enables a lower nucleation barrier and a faster Li^+ ion transfer, which effectively improves the electrochemical performance of the Li metal anode. The electrochemical impedance spectrum (EIS) was also recorded to examine the charge transfer impedance at the interface between the electrode and electrolyte. The Nyquist plot shown in Fig. 8d shows the EIS fitted results according to the equivalent circuit (Fig. 8e). In the high-frequency region, R_e represents the

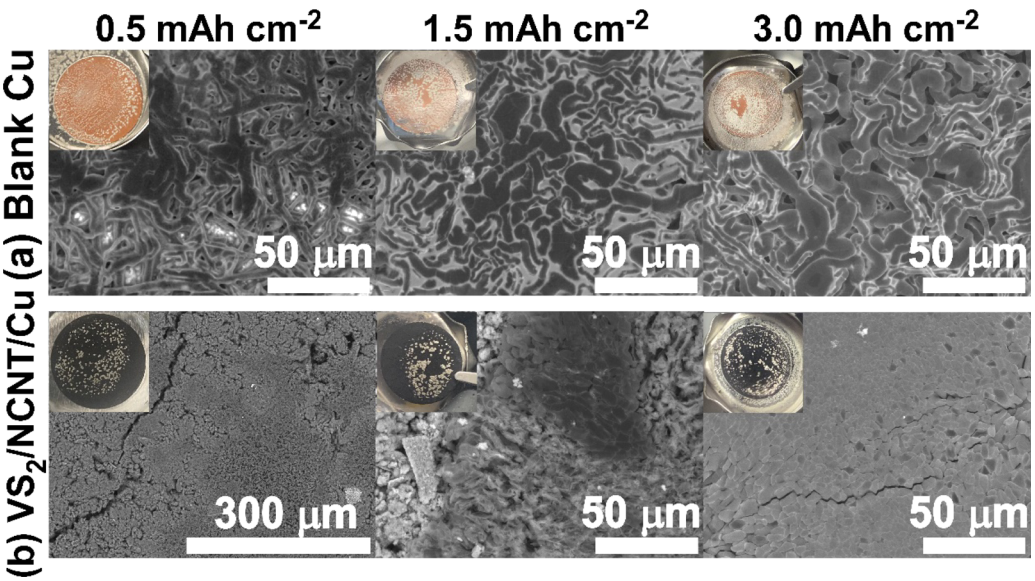

Fig. 7 Investigations of Li electrodeposition behaviors. The morphology of Li plating by SEM on (a) blank Cu and (b) VS_2/NCNT/Cu with the capacity of 0.5 mA h cm^{-2}, 1.5 mA h cm^{-2} and 3.0 mA h cm^{-2} at 10 mA cm^{-2}. The insets are the optical images of the disassembled electrode after the Li plating process. Li deposition on VS_2/NCNT/Cu is smooth and compact, without the dendrite formation.

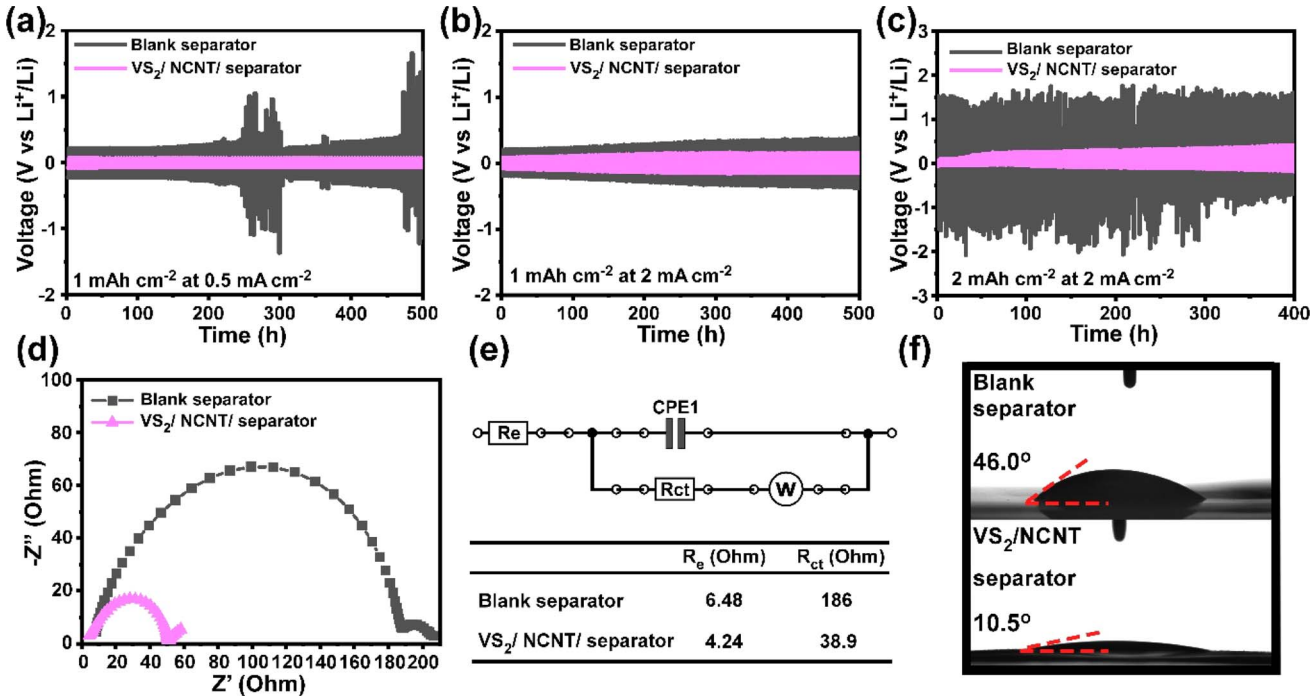

	R_e (Ohm)	R_{ct} (Ohm)
Blank separator	6.48	186
VS_2/ NCNT/ separator	4.24	38.9

Fig. 8 Electrochemical performances of the symmetric cells and the comparison of electrolyte wettability between blank and VS_2/NCNT/separator. Voltage profiles of Li plating and stripping in Li/Li symmetric cells at the current densities of (a) 0.5 mA cm^{-2} and (b) 2 mA cm^{-2} with the deposition capacity of 1 mA h cm^{-2} and (c) 2 mA cm^{-2} with deposition capacity of 2 mA h cm^{-2}. (d) Electrochemical impedance spectra (EIS) of blank and VS_2/NCNT/separator. (e) EIS corresponding equivalent circuit and the result table. (f) Contact angle test of the blank separator and the VS_2/NCNT/separator. The cell cyclability with VS_2/NCNT was extremely stable over 1000 cycles with small internal resistance and good electrolyte wettability.

resistance of Li ions passing through the cell components of the electrolyte.[36] The similar R_e values indicate identical testing conditions and cell preparation procedures. In the lower frequency region, R_{ct} is referred to as the resistance of ion transfer through the interface between the electrolyte and electrode[37] and the VS_2/NCNT/separator enables a significantly lower R_{ct} of 38.9 Ω, compared to the blank separator of 186 Ω. This suggests a better cell kinetics with the VS_2/NCNT/separator, attributed to the low diffusion barrier and high Li^+ ion conductivity, which can be explained by the wettability test results shown in Fig. 8f. The electrolyte droplet instantly spreads on the VS_2/NCNT/separator with a contact angle of 10.5°. In a sharp contrast, the droplet remains on the blank PP separator with the angle of 46.0°. The enhanced electrolyte wettability facilitates the charge/ion transport and improves the electrochemical performance. Distinct XRD peaks found in Fig. S6† indicated the high crystallinity of VS_2 after 100 cycles of symmetric cell testing, indicating good stability of VS_2 in the composite.

To show the practical use of VS_2/NCNT in the Li metal full cell, the VS_2/NCNT composite was firstly melt-diffused with ~58% of sulfur (Fig. S7†), denoted as VS_2/NCNT/S, as the cathode materials for LSB, while the VS_2/NCNT was also coated on a separator for the Li metal anode. The battery configuration is schematically displayed in Fig. S8a.† The galvanostatic charge–discharge profile shown in Fig. S8b† indicates that the pure S electrode delivers a low discharge capacity of 667 mA h g^{-1} at 0.05C in the 1st cycle. In sharp contrast, a significantly higher capacity of 1125 mA h g^{-1} is achieved with VS_2/NCNT, demonstrating an improved capacity achievement. In addition, the cycling performance shown in Fig. S8c† indicates that the cells with VS_2/NCNT/S deliver a higher initial capacity of 798 mA h g^{-1} and 99.6% coulombic efficiency over 100 cycles, while the S cell presents a much lower specific capacity with 96.2% coulombic efficiency, corresponding to 3.8% efficiency decay. The improved electrochemical performance can be explained by the Li_2S_6 adsorption test data shown in Fig. S9.† In the test, the same amounts of VS_2/NCNT and NCNT were immersed into the as-prepared 0.01 M Li_2S_6 solution. Significant color fading of VS_2/NCNT with higher light transmittance at 560 nm wavelength confirmed its better LiPS anchoring ability.

3. Conclusions

The lithiophilicity chemistry of the layered metal sulfides/selenides as the heterogeneous Li deposition substrate was probed using the first principle and experimental methods. We found that 1T transition metal sulfides and selenides enabled a strong Li affinity and high diffusion rate. VS_2 was taken as an example to represent the 1T TMDs for the Bader charge analysis and experimental section. The high lithiophilicity was confirmed by the Bader charge analysis that the 0.032 e$^-$ per atom charges were transferred from VS_2 to Li^+, also driven by

the ion-dipole force induced between the V and S atoms that are quantitatively validated by a descriptor related to the charge density and metal electronegativity. SEM characterization verified a smoother and more compact Li electrodeposition on VS_2/NCNT/Cu, while massive Li dendrites were discovered on blank Cu. The electrochemical performance in the Li/Li symmetric cell found a stable cycling with reduced overpotentials of 75 and 12 mV at 0.5 mA cm^{-2} and 2 mA cm^{-2}, respectively, over 1000 hours. Our work reveals the lithiophilic properties of transition metal sulfides and selenides that help to regulate Li growth direction and eventually solve the dendrite problem with a reduced Li diffusion barrier, providing insights into the development of stable metal batteries technology.

Data availability

The data supporting this article have been included as part of the ESI.†

Conflicts of interest

There are no conflicts to declare.

Acknowledgements

Z. L. acknowledge supports by Research Grant Council (RGC) of Hong Kong SAR (No. 16304421), and the IER Foundation (HT-JD-CXY-201907), Guangdong Science and Technology Department (Project#: 2020A0505090003), Guangdong-Hong Kong-Macao Joint Laboratory for Intelligent Micro-Nano Optoelectronic Technology (No. 2020B1212030010), and Shenzhen Special Fund for Central Guiding the Local Science and Technology Development (2021Szvup136). Technical assistance from the Materials Characterization and Preparation Facilities, Nanosystem Fabrication Facility of HKUST is greatly appreciated.

References

1 W. Ren, Y. Zheng, Z. Cui, Y. Tao, B. Li and W. Wang, Recent progress of functional separators in dendrite inhibition for lithium metal batteries, *Energy Storage Mater.*, 2021, **35**, 157–168.
2 X.-R. Chen, B.-C. Zhao, C. Yan and Q. Zhang, Review on Li Deposition in Working Batteries: From Nucleation to Early Growth, *Adv. Mater.*, 2021, **33**, 2004128.
3 W. Xu, J. Wang, F. Ding, X. Chen, E. Nasybulin, Y. Zhang and J.-G. Zhang, Lithium metal anodes for rechargeable batteries, *Energy Environ. Sci.*, 2014, **7**, 513–537.
4 K. N. Wood, M. Noked and N. P. Dasgupta, Lithium Metal Anodes: Toward an Improved Understanding of Coupled Morphological, Electrochemical, and Mechanical Behavior, *ACS Energy Lett.*, 2017, **2**, 664–672.
5 J. H. Lee, H. Lee, J. Lee, T. W. Kang, J. H. Park, J. H. Shin, H. Lee, D. Majhi, S. U. Lee and J. H. Kim, Multicomponent Covalent Organic Framework Solid Electrolyte Allowing Effective Li-Ion Dissociation and Diffusion for All-Solid-State Batteries, *ACS Nano*, 2023, **17**, 17372–17382.
6 Z. Li, Z.-W. Liu, Z. Li, T.-X. Wang, F. Zhao, X. Ding, W. Feng and B.-H. Han, Defective 2D Covalent Organic Frameworks for Postfunctionalization, *Adv. Funct. Mater.*, 2020, **30**, 1909267.
7 M. J. Lee, J. Han, K. Lee, Y. J. Lee, B. G. Kim, K.-N. Jung, B. J. Kim and S. W. Lee, Elastomeric electrolytes for high-energy solid-state lithium batteries, *Nature*, 2022, **601**, 217–222.
8 X.-B. Cheng, R. Zhang, C.-Z. Zhao and Q. Zhang, Toward Safe Lithium Metal Anode in Rechargeable Batteries: A Review, *Chem. Rev.*, 2017, **11**, 10403–10473.
9 B. M. I. Rao, R. W. Francis and H. A. Christopher, Lithium-Aluminum Electrode, *J. Electrochem. Soc.*, 1977, **124**, 1490–1492.
10 H. Kim, J. T. Lee, D.-C. Lee, M. Oschatz, W. I. Cho, S. Kaskel and G. Yushin, Enhancing performance of Li–S cells using a Li–Al alloy anode coating, *Electrochem. Commun.*, 2013, **36**, 38–41.
11 X. Zhang, W. Wang, A. Wang, Y. Huang, K. Yuan, Z. Yu, J. Qiu and Y. Yang, Improved cycle stability and high security of Li-B alloy anode for lithium–sulfur battery, *J. Mater. Chem. A*, 2014, **2**, 11660–11665.
12 T. J. Richardson and G. Chen, Solid solution lithium alloy cermet anodes, *J. Power Sources*, 2007, **174**, 810–812.
13 E. Markevich, G. Salitra, F. Chesneau, M. Schmidt and D. Aurbach, Very Stable Lithium Metal Stripping–Plating at a High Rate and High Areal Capacity in Fluoroethylene Carbonate-Based Organic Electrolyte Solution, *ACS Energy Lett.*, 2017, **2**, 1321–1326.
14 X.-Q. Zhang, X. Chen, X.-B. Cheng, B.-Q. Li, X. Shen, C. Yan, J.-Q. Huang and Q. Zhang, Highly Stable Lithium Metal Batteries Enabled by Regulating the Solvation of Lithium Ions in Nonaqueous Electrolytes, *Angew. Chem.*, 2018, **130**, 5399–5403.
15 J. Zheng, M. H. Engelhard, D. Mei, S. Jiao, B. J. Polzin, J.-G. Zhang and W. Xu, Electrolyte additive enabled fast charging and stable cycling lithium metal batteries, *Nat. Energy*, 2017, **2**, 17012.
16 L. Gireaud, S. Grugeon, S. Laruelle, B. Yrieix and J.-M. Tarascon, Lithium metal stripping/plating mechanisms studies: A metallurgical approach, *Electrochem. Commun.*, 2006, **8**, 1639–1649.
17 Y. Liu, Q. Liu, L. Xin, Y. Liu, F. Yang, E. A. Stach and J. Xie, Making Li-metal electrodes rechargeable by controlling the dendrite growth direction, *Nat. Energy*, 2017, **2**, 17083.
18 C.-P. Yang, Y.-X. Yin, S.-F. Zhang, N.-W. Li and Y.-G. Guo, Accommodating lithium into 3D current collectors with a submicron skeleton towards long-life lithium metal anodes, *Nat. Commun.*, 2015, **6**, 8058.
19 C. Monroe and J. Newman, Dendrite Growth in Lithium/Polymer Systems: A Propagation Model for Liquid Electrolytes under Galvanostatic Conditions, *J. Electrochem. Soc.*, 2003, **150**, A1377–A1384.
20 F. Guo, C. Wu, H. Chen, F. Zhong, X. Ai, H. Yang and J. Qian, Dendrite-free lithium deposition by coating a lithiophilic

heterogeneous metal layer on lithium metal anode, *Energy Storage Mater.*, 2020, **24**, 635–643.

21 F. Chu, J. Hu, J. Tian, X. Zhou, Z. Li and C. Li, *In Situ* Plating of Porous Mg Network Layer to Reinforce Anode Dendrite Suppression in Li-Metal Batteries, *ACS Appl. Mater. Interfaces*, 2018, **10**, 12678–12689.

22 K. Yan, Z. Lu, H.-W. Lee, F. Xiong, Po-C. Hsu, Y. Li, J. Zhao, S. Chu and Y. Cui, Selective deposition and stable encapsulation of lithium through heterogeneous seeded growth, *Nat. Energy*, 2016, **1**, 16010.

23 P. Zhai, T. Wang, W. Yang, S. Cui, P. Zhang, A. Nie, Q. Zhang and Y. Gong, Uniform Lithium Deposition Assisted by Single-Atom Doping toward High-Performance Lithium Metal Anodes, *Adv. Energy Mater.*, 2019, **9**, 1804019.

24 R. Zhang, X.-R. Chen, X. Chen, X.-B. Cheng, X.-Q. Zhang, C. Yan and Q. Zhang, Lithiophilic Sites in Doped Graphene Guide Uniform Lithium Nucleation for Dendrite-Free Lithium Metal Anodes, *Angew. Chem.*, 2017, **129**, 7872–7876.

25 J. Wu, H. Zeng, X. Li, X. Xiang, Y. Liao, Z. Xue, Y. Ye and X. Xie, Ultralight Layer-by-Layer Self-Assembled MoS_2-Polymer Modified Separator for Simultaneously Trapping Polysulfides and Suppressing Lithium Dendrites, *Adv. Energy Mater.*, 2018, **8**, 1802430.

26 M. Jackle, K. Helmbrecht, M. Smits, D. Stottmeister and A. Groß, Self-diffusion barriers: possible descriptors for dendrite growth in batteries?, *Energy Environ. Sci.*, 2018, **11**, 3400–3407.

27 Y. Lu, Z. Tu and L. A. Archer, Stable lithium electrodeposition in liquid and nanoporous solid electrolytes, *Nat. Mater.*, 2014, **13**, 962–969.

28 N. Xu, L. Li, Y. He, Y. Tong and Y. Lu, Understanding the molecular mechanism of lithium deposition for practical high-energy lithium-metal batteries, *J. Mater. Chem. A*, 2020, **8**, 6229–6237.

29 H. Wong, X. Ou, M. Zhuang, Z. Liu, M. D. Hossain, Y. Cai, H. Liu, H. Lee, C.-Z. Wang and Z. Luo, Selenium Edge as a Selective Anchoring Site for Lithium–Sulfur Batteries with $MoSe_2$/Graphene-Based Cathodes, *ACS Appl. Mater. Interfaces*, 2019, **11**, 19986–19993.

30 P. He, M. Yan, G. Zhang, R. Sun, L. Chen, Q. An and L. Mai, Layered VS_2 Nanosheet-Based Aqueous Zn Ion Battery Cathode, *Adv. Energy Mater.*, 2017, **7**, 1601920.

31 S. Zhang, J. Wang, N. L. Torad, W. Xia, M. A. Aslam, Y. V. Kaneti, Z. Hou, Z. Ding, B. Da, A. Fatehmulla, A. M. Aldhafiri, W. A. Farooq, J. Tang, Y. Bando and Y. Yamauchi, Rational Design of Nanoporous MoS_2/VS_2 Heteroarchitecture for Ultrahigh Performance Ammonia Sensors, *Small*, 2020, **16**, 1901718.

32 Z. Liu, A. Daali, G.-L. Xu, M. Zhuang, X. Zuo, C.-J. Sun, Y. Liu, Y. Cai, M. D. Hossain, H. Liu, K. Amine and Z. Luo, Highly Reversible Sodiation/Desodiation from a Carbon-Sandwiched SnS_2 Nanosheet Anode for Sodium Ion Batteries, *Nano Lett.*, 2020, **20**, 3844–3851.

33 X. Liang, M. Chen, H. Zhu, H. Zhu, X. Cui, J. Yan, Q. Chen, X. Xia and Q. Liu, Unveiling the solid-solution charge storage mechanism in 1T vanadium disulfide nanoarray cathodes, *J. Mater. Chem. A*, 2020, **8**, 9068–9076.

34 Z. Cheng, Z. Xiao, H. Pan, S. Wang and R. Wang, Elastic Sandwich-Type rGO–VS_2/S Composites with High Tap Density: Structural and Chemical Cooperativity Enabling Lithium–Sulfur Batteries with High Energy Density, *Adv. Energy Mater.*, 2017, **8**, 1702337.

35 H. Liang, H. Shi, D. Zhang, F. Ming, R. Wang, J. Zhuo and Z. Wang, Solution Growth of Vertical VS_2 Nanoplate Arrays for Electrocatalytic Hydrogen Evolution, *Chem. Mater.*, 2016, **28**, 5587–5591.

36 M. Xu, Y. Li, M. Ihsan-Ul-Haq, N. Mubarak, Z. Liu, J. Wu, Z. Luo and J. K. Kim, NaF-rich solid electrolyte interphase for dendrite-free sodium metal batteries, *Energy Storage Mater.*, 2022, **44**, 477–486.

37 S. Yao, J. Cui, J.-Q. Huang, Z. Lu, Y. Deng, W. G. Chong, J. Wu, M. I. U. Haq, F. Ciucci and J.-K. Kim, Novel 2D Sb_2S_3 Nanosheet/CNT Coupling Layer for Exceptional Polysulfide Recycling Performance, *Adv. Energy Mater.*, 2018, **8**, 1800710.

